Overview of Torque Ripple Minimization Methods for Permanent Magnet Synchronous Motors Based on Harmonic Injection*

Peng Yi, *Wenzhi Zheng and Xianglin Li**

(College of Electrical Engineering, Qingdao University, Qingdao 266071, China)

Abstract: Permanent magnet synchronous motors (PMSMs) are widely used because of their high power/torque density and high efficiency, particularly in applications with strict requirements for arrangement space or weight, such as in the electric vehicle (EV) and aerospace fields. Recently, the PMSM torque ripple problem has received increasing interest because PMSM drive requirements continuously improve. For applications with complex transmission and a wide speed range, torque ripple can easily cause system resonance, which deteriorates the driving performance. The research status and latest progress in the minimization of PMSM torque ripple based on harmonic injection are discussed. First, the causes of PMSM torque ripple are analyzed. Subsequently, the research status of the PMSM analytical model is introduced, and multiple current harmonic control and optimization methods are described in detail. Finally, future development trends in this field are analyzed.

Keywords: Permanent magnet synchronous motor, torque ripple minimization, harmonic injection

1 Introduction

Under the challenges of economic development and environmental protection, electric vehicles (EVs) have become a strategic option for the development of China's automobile industry. The proposal of the "Development plan for the new energy vehicle industry (2021—2035)" marks a new era in the Chinese automobile industry. Owing to the limited layout space of EVs and the demand for high power/torque densities, permanent magnet synchronous motors (PMSMs) are prominent as mainstream products. High power density implies high magnetic saturation; therefore, the torque ripple problem is more prevalent. The complexity of the EV powertrain and its wide speed range make it prone to resonance. Therefore, for EV motors, the torque ripple problem must be addressed urgently.

Torque ripple minimization methods are divided into two main categories: one is based on the electromagnetic structure optimization and the other one is based on control. Methods based on electromagnetic structure optimization primarily include optimizing the stator structure [1], rotor structure [2-3], air gap structure [4-6], winding form, and pole-slot matching [7]. Although this type of method can suppress torque ripple well, the following problems occur: first, the torque ripple caused by the inverter factor cannot be eliminated; second, some methods (such as stator skew and rotor skew) produce axial forces and reduce the power/torque density; third, these methods are generally only applicable to newly manufactured motors.

Methods based on control can solve the above problems; thus, they have become popular in research on torque ripple minimization. However, torque ripple minimization based on harmonic injection produces many problems. For example, an accurate torque ripple analytical model is required to express torque harmonics, accurate PMSM lumped parameters (including harmonic parameters) are required, optimized injected current harmonics must be obtained, and the negative effects caused by injected current harmonics should be considered. All these challenges

Manuscript received August 8, 2023; revised September 29, 2023; accepted October 15, 2023. Date of publication June 30, 2024; date of current version November 7, 2023.

* Corresponding Author, E-mail: lxllcc@126.com

* Supported in part by the National Natural Science Foundation of China (52107052), in part by the Natural Science Foundation of Shandong Province (ZR2021QE222 and ZR2021YQ33).

Digital Object Identifier: 10.23919/CJEE.2023.000045

are significant topics in current research. In this paper, the latest research progress and the main technical difficulties in PMSM torque ripple minimization based on harmonic injection are summarized and analyzed to provide guidance for PMSM torque ripple minimization.

Section 2 analyzes the causes of PMSM torque ripple. The research status of the PMSM torque ripple analytical model is presented in Section 3. The problems in the research on PMSM torque ripple minimization based on harmonic injection are summarized in Section 4, including multiple current harmonic control and current harmonic optimization methods, which are elaborated in detail.

2 Causes of torque ripple

Torque ripple in PMSMs is caused by many factors. A structural diagram of a traditional PMSM field orientation control (FOC) system is shown in Fig. 1. The causes of torque ripple in this system can be summarized as inverter, motor, control, and sensor factors.

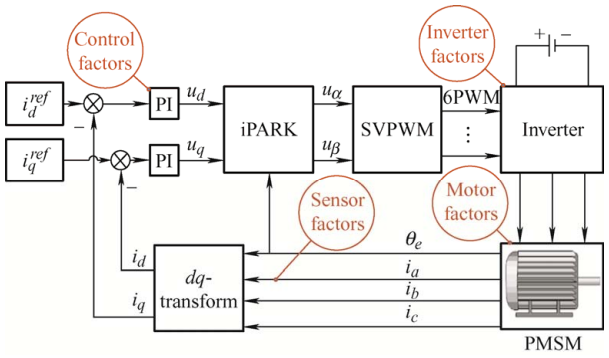

Fig. 1 Torque ripple produced in a traditional PMSM FOC system

2.1 Inverter factors

Insulated gate bipolar transistors (IGBTs) are widely used as power switching devices in EV inverters. During the IGBT turn-off process, current tailing occurs owing to the difficulty in eliminating the stored charge. To prevent a short circuit caused by the simultaneous conduction of the upper and lower bridge arms during the turn-off process, the IGBT is set to delay the conduction, and the delay time is called the dead time. Owing to the incorporation of dead time, the phase current causes a current clamp phenomenon because of the lack of voltage when the phase current crosses zero; thus, current harmonics are introduced [8-9], as shown in Fig. 2a. Various dead-time compensation methods have been proposed [10-12]. For IGBT inverters, the current tailing phenomenon is more severe; therefore, the dead time must be larger, which results in larger current harmonics. The new high-speed switching device, the SiC MOSFET, has a short turn-off time and can be used with a short dead time, which can effectively reduce the current harmonics and obtain a higher switching frequency. Therefore, SiC MOSFET inverters are being increasingly used. In addition, a conduction voltage drop occurs when the switching elements and diodes of the inverter are on, which is known as the tube voltage drop [13]. Because of the tube voltage drop, the voltage applied to the motor phase winding produces a certain deviation. This also distorts the phase voltage waveform, resulting in current waveform distortion [13-14].

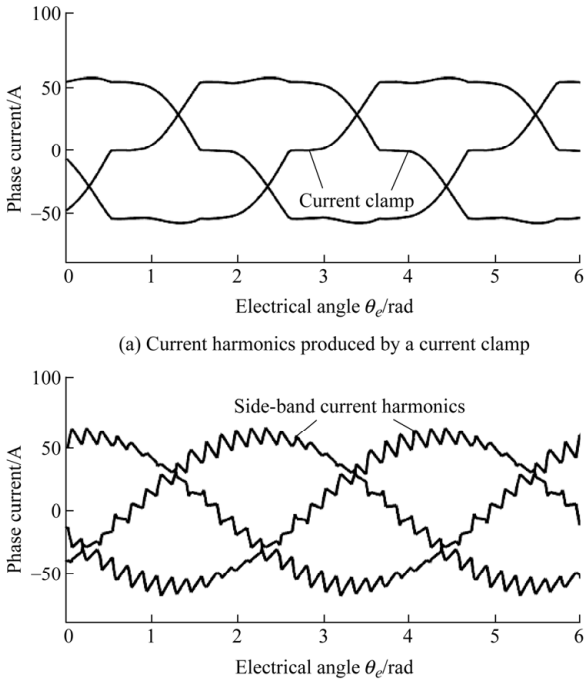

(a) Current harmonics produced by a current clamp

(b) Side-band current harmonics produced by modulation

Fig. 2 Current harmonics produced by an inverter

In addition, the voltage harmonics around the integer multiple switching frequency (also called side-band voltage harmonics) generated by modulation also cause current harmonics (side-band current harmonics) [15-16]. This type of harmonics causes torque ripple. This phenomenon is more significant

with low carrier ratio modulation [17]. Current harmonics with low carrier ratio modulation are shown in Fig. 2b. Side-band harmonics have a higher frequency and are typically suppressed by modifying the modulation method [18-20].

2.2 Motor factors

The torque ripple generated by a PMSM contains three main components: inductance distortion [21-24], permanent magnet (PM) flux distortion [25-28], and cogging torque [29-31]. These factors are coupled with the current and ultimately form a torque ripple.

Inductance and PM flux distortions in PMSMs result from two causes: structural factors, such as stator cogging, stator winding form, anisotropy of rotor structure, and magnetic saturation. The relationship between self inductance (L_{aa}, L_{bb}, and L_{cc}), mutual inductance (L_{ab}, L_{ba}, L_{ac}, L_{ca}, L_{bc}, and L_{cb}), and electrical angle is shown in Figs. 3a and 3b, respectively. The variation in the PM flux (ψ_{fa}, ψ_{fb}, and ψ_{fc}) with the electrical angle is shown in Fig. 3c. The cogging torque of the PMSM (T_{cog}) is primarily caused by the stator cogging structure, which is closely related to the pole-slot combination of the PMSM. For integer-slot and fractional-slot PMSMs, the order of the torque ripple γ can be expressed by Eq. (1) [32-34]. The variation in the cogging torque with the electrical angle for an integer-slot PMSM is shown in Fig. 3d.

$$\gamma = 2pZ/\mathrm{GCD}(Z,2p) = \mathrm{LCM}(Z,2p) \tag{1}$$

where p is the number of pole pairs, Z is the number of stator slots, $\mathrm{GCD}(\bullet)$ is the greatest common divisor, and $\mathrm{LCM}(\bullet)$ is the least common multiple.

In addition to the above factors, control and sensor factors cause torque ripples in the PMSM. For example, an incomplete symmetry of each phase structure during the motor manufacturing process can cause phase current asymmetry. An asymmetric phase current generates a negative sequence component of the fundamental wave [35-36]. In the control process, this negative sequence component is not attenuated because the PI controller has a certain bandwidth that generates a low-order torque ripple. In addition, sampling errors in a current sensor can also cause this type of problem.

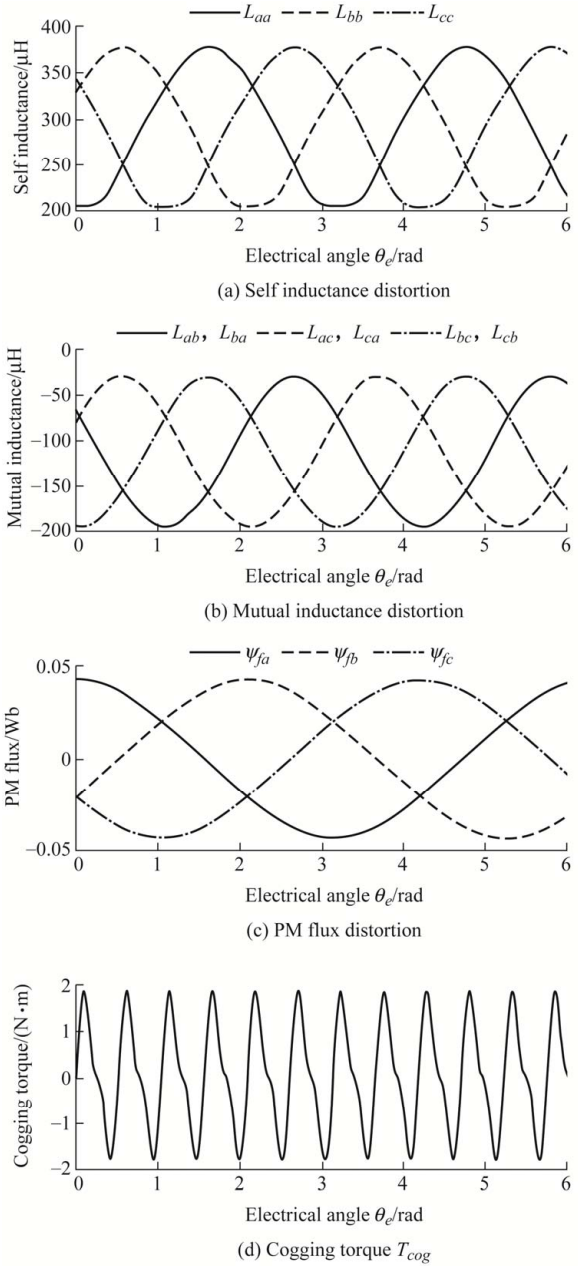

Fig. 3 Parameter distortion and cogging torque of PMSM

3 Research on PMSM torque analytical models

The numerical models of a PMSM include finite element (FE) and parametric analytical models. The FE model can be used to obtain the voltage, flux, and torque through physical structure modeling, meshing, and FE calculations. The modeling of this method is more intuitive, and the calculation result is more accurate, making it suitable for the PMSM design stage. However, the number of calculations required is large, making it unsuitable for online system simulations. The parametric analytical model is used

to express the flux, voltage, and torque of an actual motor by establishing an analytical model. Although the accuracy of this method is lower than that of the FE model, the calculations are fewer, which is suitable for system simulation. Moreover, with further research, the accuracy of the parametric analytical model can be significantly improved through parameter extraction.

The early analytical model of a PMSM was derived based on the balance of the input and output power [23, 37]. This class of equations primarily contains the flux linkage, voltage, and torque equations as shown in Eqs. (2)-(4), respectively.

$$\begin{cases} \psi_d = L_d i_d + \psi_f \\ \psi_q = L_q i_q \end{cases} \tag{2}$$

where i_d and i_q are the *d*-axis and *q*-axis currents, respectively; ψ_f is the PM flux linkage; ψ_d and ψ_q are the *d*-axis and *q*-axis total flux linkages, respectively.

$$\begin{cases} u_d = R_s i_d + \dfrac{\mathrm{d}\psi_d}{\mathrm{d}t} - \omega_e \psi_q \\ u_q = R_s i_q + \dfrac{\mathrm{d}\psi_q}{\mathrm{d}t} + \omega_e \psi_d \end{cases} \tag{3}$$

where u_d and u_q are *d*-axis and *q*-axis voltages, respectively, and ω_e is the electrical angular velocity.

$$T_e = \frac{3p}{2}\left[\psi_d i_q - \psi_q i_d\right] \tag{4}$$

where T_e is the torque.

Without considering the magnetic field saturation, the *d*-axis inductance, *q*-axis inductance, and PM flux linkage parameters can be considered to be constants. However, saturation occurs in the magnetic fields of PMSMs, particularly in PMSMs for EVs, where the saturation phenomenon is generally more severe when attempting to achieve a higher power density. Many scholars have investigated the analytical model of PMSMs under the condition of magnetic saturation and have made improvements to the model. Some of the results are briefly described below. In Ref. [38], considering the influence of magnetic saturation, the changes in L_d, L_q, and ψ_f of the PMSM with i_d and i_q were studied. In Ref. [39], the influence of magnetic saturation on the inductance difference between the *d*-axis and *q*-axis was analyzed and used as an independent variable in the torque ripple analytical model to improve the accuracy of the torque ripple under magnetic saturation. In Refs. [40-42], the cross-coupling effect between the *d*-axis and *q*-axis was considered; thus, mutual inductance between the *d*-axis and *q*-axis was introduced. The main cause of the cross-coupling effect is the asymmetric distribution of the magnetic field caused by magnetic saturation and the common magnetic circuit of the *d*- and *q*-axes. Similarly, the PM flux linkage ψ_f is no longer symmetrically distributed along the axis but is shifted towards the *q*-axis, resulting in a *q*-axis component ψ_{fq} [43-44]. Therefore, after considering the cross-coupling and cross-saturation effects, Eq. (2) changes as shown in the following equations: All parameters change with i_d and i_q.

$$\begin{bmatrix} \psi_d \\ \psi_q \end{bmatrix} = \begin{bmatrix} L_{dd} & L_{dq} \\ L_{qd} & L_{qq} \end{bmatrix} \begin{bmatrix} i_d \\ i_q \end{bmatrix} + \begin{bmatrix} \psi_{fd} \\ \psi_{fq} \end{bmatrix} \tag{5}$$

where L_{dd} and L_{qq} are the *d*-axis and *q*-axis self inductances, respectively; L_{dq} and L_{qd} represent the mutual inductances between the *d*-axis and *q*-axis, in which the values are equal; ψ_{fd} and ψ_{fq} represent the *d*-axis and *q*-axis components of the PM flux, respectively.

When magnetic saturation, cross-coupling, and cross-saturation are considered, Eq. (4) better reflects the average torque. However, this type of model cannot adequately reveal the energy conversion mechanism and does not include the cogging torque. A torque ripple model based on magnetic energy and magnetic co-energy was developed to better explain the energy conversion process. Ref. [37] qualitatively analyzed the magnetic energy and magnetic co-energy stored in a PMSM under no-load and load conditions and derived the relationship between torque and magnetic energy (or magnetic co-energy) under the assumption that the flux (or current) remains constant. Refs. [31-32] divided the magnetic co-energy under linear conditions into three parts: generated by the current generated by the PM and generated by the interaction between the current and the PM. A highly accurate torque ripple model was derived under linear conditions. According to the principle of virtual displacement, the torque equation can be obtained as follows

$$T_e = p\frac{\mathrm{d}W'_m}{\mathrm{d}\theta_e} = p\left(\frac{\mathrm{d}W'_{mI}}{\mathrm{d}\theta_e} + \frac{\mathrm{d}W'_{mIM}}{\mathrm{d}\theta_e} + \frac{\mathrm{d}W'_{mM}}{\mathrm{d}\theta_e}\right) \tag{6}$$

where W'_m is the magnetic co-energy, W'_{mI} is the magnetic co-energy generated by the armature current, W'_{mIM} is the magnetic co-energy generated by the interaction of the armature current and PM, and W'_{mM} is the magnetic co-energy generated by the PM.

If saturation is not considered, the parameters of the PMSM do not change with the current and are only related to the rotor position. Fig. 4 shows the curves of the armature and PM fluxes versus the current at different rotor positions. According to the definition of magnetic co-energy, $\mathrm{d}W'_{mI}/\mathrm{d}\theta_e$ exists as indicated by the shaded areas in Fig. 4a, and $\mathrm{d}W'_{mIM}/\mathrm{d}\theta_e$ exists as indicated by the shaded areas in Fig. 4b. $\mathrm{d}W'_{mM}/\mathrm{d}\theta_e$ is the changing rate of the PM magnetic co-energy with the rotor position, that is, the no-load cogging torque T_{cog}.

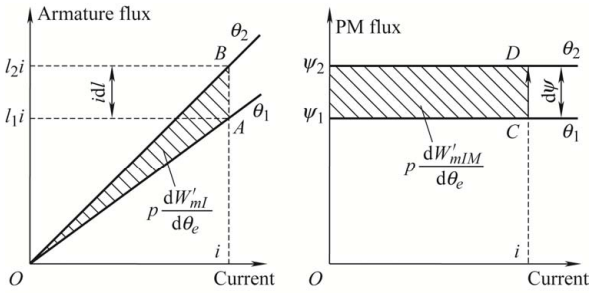

(a) $\mathrm{d}W'_{mI}/\mathrm{d}\theta_e$ (b) $\mathrm{d}W'_{mIM}/\mathrm{d}\theta_e$

Fig. 4 Variation in magnetic co-energy with rotor position

According to the geometric relationship shown in Fig. 4, the torque equation can be derived as

$$T_e = p\left(\frac{1}{2}\boldsymbol{i}_{abc}^{\mathrm{T}}\frac{\mathrm{d}\boldsymbol{L}_{abc}}{\mathrm{d}\theta_e}\boldsymbol{i}_{abc} + \boldsymbol{i}_{abc}^{\mathrm{T}}\frac{\mathrm{d}\boldsymbol{\psi}_{fabc}}{\mathrm{d}\theta_e}\right) + T_{cog} \tag{7}$$

where $\boldsymbol{i}_{abc}$ is the three-phase current vector, $\boldsymbol{\psi}_{fabc}$ is the three-phase PM flux vector, T_{cog} is the cogging torque, and $\boldsymbol{L}_{abc}$ is the three-phase inductance matrix.

In Ref. [45], an analytical model based on magnetic energy was proposed considering magnetic saturation. The variation curves of the flux when both the rotor position change ($\theta_1 \to \theta_2$) and current change ($i_A \to i_B$) are considered are indicated in Fig. 5a. The total flux is divided into the armature flux (ψ_{AM}) and no-load PM flux (ψ_{PM}). The variation in the flux ($\Delta\psi$) is divided into that caused by current variation ($\Delta\psi_i$)and that caused by rotor position variation ($\Delta\psi_\theta$). The flux component $\tilde{\psi}_{AM}$, which is used to consider the magnetic saturation, is defined by introducing an incremental inductance. The magnetic energy is also divided into three parts: S_1, S_2, and S_3, shown in Fig. 5b. S_3 is defined as $\widetilde{W}_{m\_AM}$, which is a new magnetic energy component after considering magnetic saturation. By deriving the partial derivatives of the flux and magnetic energy, $\partial\psi_{AM}/\partial i$, $\partial\psi_{AM}/\partial\theta$, and $\partial W_{m\_AM}/\partial\theta$, the torque analytical expression is finally obtained as follows

$$\begin{aligned} T_e = {} & p\boldsymbol{\rho}\left(\frac{1}{2}\boldsymbol{i}_{dq0}^{\mathrm{T}}\boldsymbol{L}_C\boldsymbol{i}_{dq0} + \frac{1}{2}\boldsymbol{i}_{dq0}^{\mathrm{T}}\frac{\mathrm{d}\boldsymbol{L}_{dq0}}{\mathrm{d}\theta_e}\boldsymbol{i}_{dq0}\right) + \\ & p\boldsymbol{\rho}\boldsymbol{i}_{dq0}^{\mathrm{T}}\left(\frac{\mathrm{d}\widetilde{\boldsymbol{\psi}}_{AM\_dq0}}{\mathrm{d}\theta_e} + \frac{\mathrm{d}\boldsymbol{\psi}_{PM\_dq0}}{\mathrm{d}\theta_e} + \boldsymbol{\gamma}\widetilde{\boldsymbol{\psi}}_{AM\_dq0} + \boldsymbol{\gamma}\boldsymbol{\psi}_{PM\_dq0}\right) - \\ & p\left(\frac{\mathrm{d}\widetilde{W}_{m\_AM}}{\mathrm{d}\theta_e} + \frac{\mathrm{d}W_{m\_PM}}{\mathrm{d}\theta_e}\right) \end{aligned} \tag{8}$$

where $\boldsymbol{L}_{dq0}$ is the incremental inductance matrix in the $dq0$ coordinate; $\boldsymbol{\psi}_{PM\_dq0}$ is the no-load PM flux vector in the $dq0$ coordinate; W_{m_PM} is the no-load PM magnetic energy; $\widetilde{\boldsymbol{\psi}}_{AM\_dq0}$ and $\widetilde{W}_{m\_AM}$ are the flux and magnetic energy components introduced by magnetic saturation, respectively; $\boldsymbol{L}_C = \boldsymbol{\gamma}\boldsymbol{L}_{dq0} - \boldsymbol{L}_{dq0}\boldsymbol{\gamma}$; $\boldsymbol{\rho} = diag\left(\frac{3}{2},\frac{3}{2},3\right)$; $\boldsymbol{\gamma} = \begin{bmatrix} 0 & -1 & 0 \\ 1 & 0 & 0 \\ 0 & 0 & 0 \end{bmatrix}$.

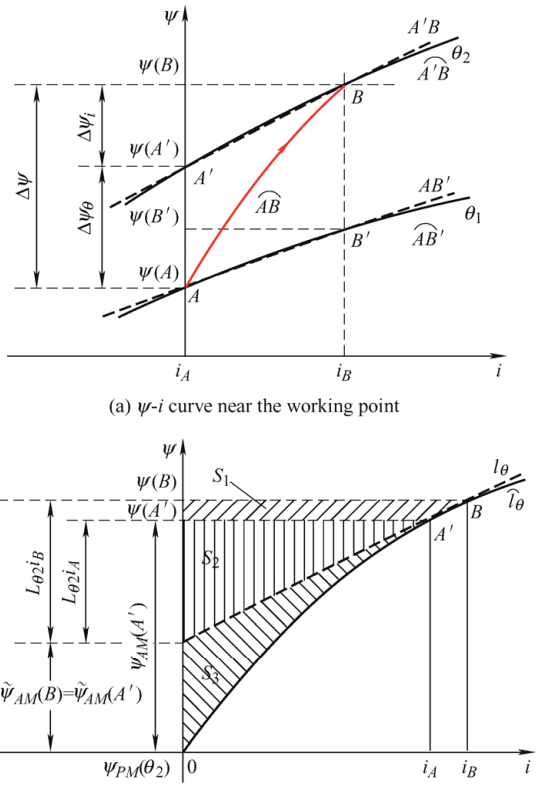

(a) ψ-i curve near the working point

(b) Relationship between ψ and magnetic energy under θ_2

Fig. 5 Magnetic energy analysis near the working point

In addition, other types of analytical torque models exist. In Ref. [46], from the perspective of numerical

solutions, FE analysis was used to establish a magnetic co-energy database under different current amplitude angles and rotor positions, and the torque analytical model was established using 2D Fourier analysis. In Refs. [47-48], an analytical model of torque was established using the Maxwell tensor equations.

4 PMSM torque ripple minimization based on harmonic injection

The torque ripple minimization methods based on the control described in Section 1 primarily refer to suppressing the torque ripple through harmonic injection, and the involved challenges primarily include the harmonic injection method and current harmonic optimization.

4.1 Methods of harmonic injection

For the traditional FOC method, in the *dq* coordinate, the fundamental currents are transformed into the *d*-axis and *q*-axis DC components using Clark and Park transformation. Subsequently, the DC components can be tracked without a steady state error using closed-loop proportional-integral (PI) control. However, the current harmonics are still AC components in the *dq* coordinate although their orders change due to the coordinate transformation. Taking the steady-state as an example, if the used pulse width modulation (PWM) method is symmetrical, the generated voltage harmonics contain only odd harmonics (1^{st}, 3^{rd}, 5^{th}, 7^{th}, ⋯). If the stator winding of the PMSM is the most commonly used three-phase "Y" type with no center connection, the voltage harmonics that are multiples of 3 (also called the zero sequence components) generated through PWM will not cause current harmonics of these orders. Therefore, the current harmonic orders can be summarized as $6n\pm1(n\in N^{+})$, where the $(6n-1)^{th}$ harmonics are the negative sequence components, and the $(6n+1)^{th}$ harmonics are positive sequence components. After coordinate transformation, the $(6n\pm1)^{th}$ harmonics in the phase current become $6n^{th}$ harmonics in the *dq* coordinate. Therefore, the methods of harmonic injection can be divided into AC and DC signal control. Common AC signal control methods include hysteresis current control, proportional resonance (PR) control, and repetitive control. The DC signal control method primarily refers to the control based on the multiple reference frame (MRF).

4.1.1 Hysteresis loop current control

In Ref. [29], the current harmonics were controlled using hysteresis-loop PWM technology. The control block diagram is shown in Fig. 6. This method must be implemented using an analog-to-comparison circuit. It is easily affected by current sensor noise, which causes continuous switching. The current control accuracy is significantly affected by the width of the hysteresis-loop band: the larger the hysteresis bandwidth, the lower the current control accuracy; the smaller the width of the hysteresis band, the higher the switching frequency. In Fig. 6, $\overline{i_a^{ref}}$, $\overline{i_b^{ref}}$, and $\overline{i_c^{ref}}$ are the fundamental components of the reference phase current, and i_{ah}^{ref}, i_{bh}^{ref}, and i_{ch}^{ref} are the harmonic components of the reference phase current.

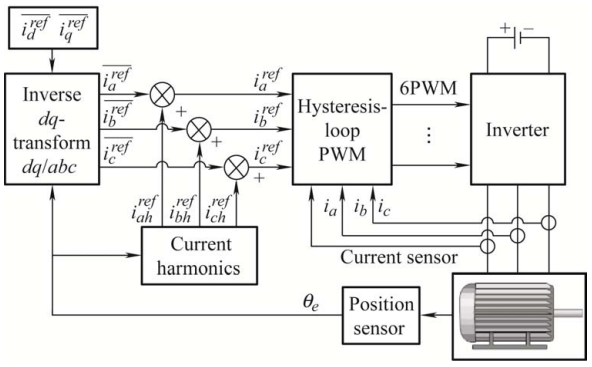

Fig. 6 Current harmonic control using hysteresis-loop PWM

4.1.2 Repetitive control

In Refs. [23, 49], the current harmonics were controlled using repetitive control. The concept of repetitive control is derived from internal model control [50]. Internal model control entails that the system can track reference inputs without a steady-state error if the closed-loop system contains a model that can generate these reference inputs. Repetitive control exploits this principle. If the reference inputs are significantly periodic, the signal error is delayed by one cycle and applied as feedback to the forward channel. Thus, the closed-loop system satisfies the conditions for the internal mode control. The current harmonic control block diagram used in Ref. [23] is shown in Fig. 7a, where the current repetition controller is indicated as REP; its specific structure is shown in Fig. 7b.

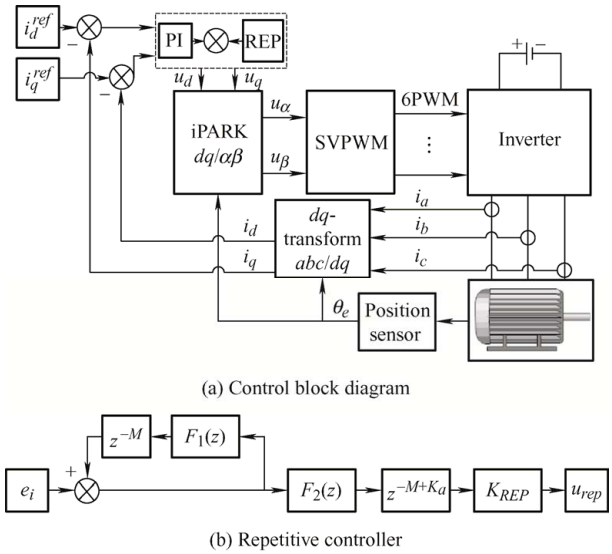

(a) Control block diagram

(b) Repetitive controller

Fig. 7 Current harmonic control using a repetitive controller

In Fig. 7b, $F_1(z)$ and $F_2(z)$ are low-pass filters used to eliminate high frequency noise and prevent it from causing system instability owing to positive feedback. K_{REP} is the controller gain, M is the period of the reference input, and K_a is the advance adjustment used to increase the stability margin of the system [49].

4.1.3 Proportional resonance control

In Refs. [39, 51-54], current harmonics were controlled using proportional resonant control. Strictly, proportional resonant control is derived from the internal model control. If the controller contains the transfer function of the sinusoidal function, it can control the sinusoidal reference signal at the same frequency without steady-state errors. The transfer function of the proportional resonant controller is expressed as

$$G_{PR}(s)=K_p+\frac{K_r s}{s^2+\omega_0^2} \tag{9}$$

where K_p is the proportion coefficient, K_r is the resonance coefficient, and ω_0 is the resonant frequency.

The transfer function shown in Eq. (9) is the transfer function of an ideal proportional resonant controller. Its amplitude-frequency characteristic is that the amplitude at the frequency ω_0 is infinite, and the amplitude at the other frequency positions is zero, as shown in Fig. 8. However, an ideal controller cannot be applied in practice because when the frequency estimation deviates slightly, the proportional resonance controller will not function. To overcome this limitation, the ideal proportional resonant controller is generally deformed such that the proportional resonant controller has a certain bandwidth, as shown by the dash-dot, dashed, and dotted lines in Fig. 8. The proportional resonant controller with a certain bandwidth is expressed as

$$G_{PR}(s)=K_p+\frac{K_r\omega_c s}{s^2+2\omega_c s+\omega_0^2} \tag{10}$$

where ω_c is the cut-off frequency.

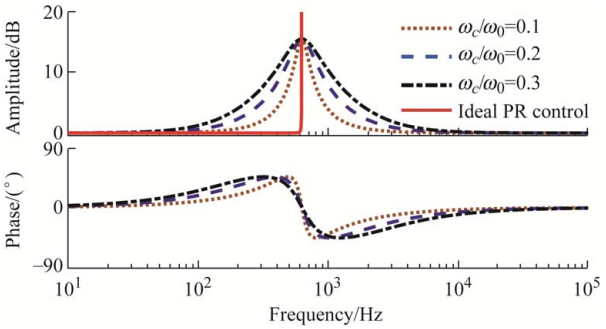

Fig. 8 Bode diagram of the PR controller under different parameters

As shown in Fig. 8, the amplitude-frequency curve of the proportional resonant controller has a certain bandwidth after ω_c is added, and the larger the ω_c, the larger the bandwidth. Therefore, a small deviation in the frequency estimation can be controlled effectively. However, two problems are caused by this addition: first, the increase of frequency bandwidth inevitably causes harmonics or noise of other frequencies to respond; therefore, the appropriate bandwidth should be selected; second, the gain at the resonant frequency ω_0 is a finite rather than infinite value, which makes the steady state error appear at this frequency. The higher the gain, the smaller the steady-state error, which means that the harmonic injection will be more accurate; however, it will also cause instability in the control.

4.1.4 Harmonic control based on MRF transform

In Ref. [55], a harmonic control method based on MRF coordinate transformation was proposed. This method extends the traditional FOC to the harmonic category. Through n^{th} synchronous coordinate transformation, the n^{th} three-phase current harmonic is decomposed into i_{dn} and i_{qn}, which are DC components, and the interference is then filtered using low-pass filtering to obtain the DC component.

Because the specific harmonics are transferred to the DC component after the coordinate transformation, they can be controlled using PI control. The control structure when PI controllers are used to control the 5^{th} and 7^{th} harmonics is shown in Fig. 9. This method has the advantages of no steady-state errors, easy selection of control parameters, and strong robustness. However, the calculations are numerous because of the coordinate transformations and filtering processes. In Refs. [56-57], the relationship between current and voltage harmonics was investigated, and the coupling effect between them was reduced to some extent in the control method used.

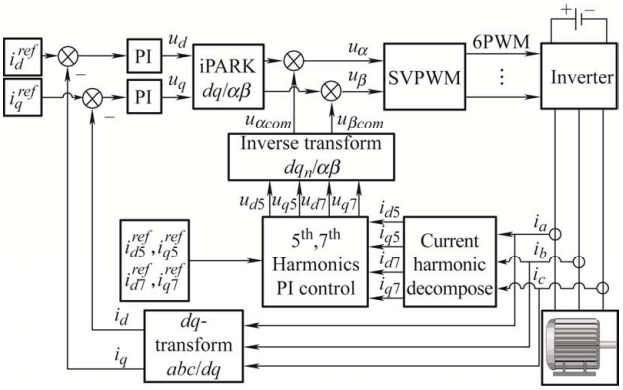

Fig. 9 Multiple reference frame PI control block diagram

After n^{th} coordinate transformation, i_{dn} and i_{qn} become DC components, while the fundamental current becomes a high-order component with a large amplitude, which requires a large filtering time constant to filter out this component. A large filtering time constant indicates a large phase delay in control. Although i_{dn} and i_{qn} become DC components and do not affect the control accuracy, a phase delay occurs in the process of dynamic adjustment, which affects the stability of the control. This makes it much more difficult to stabilize the higher-order harmonic controller. In Refs. [58-60], the coupling relationship between the voltage harmonics and current harmonics was further derived, the robustness of the control system was investigated based on the harmonic control state equation, and controllers that can maintain good robustness over the entire speed range and full current MAP were designed.

4.1.5 Model predictive control

Previous methods of harmonic control were designed to inject harmonics to eliminate torque ripple by implementing closed-loop control of the current, which is more likely to be the expansion of the FOC in harmonic control. In addition to the above closed-loop harmonic control method, another type of control for torque ripple minimization is model predictive control. Model predictive control is similar to direct torque control (DTC) in principle. By establishing a prediction equation for the current, flux, torque, and voltage, an appropriate voltage vector is selected to reduce the errors of the torque and flux [61-69]. The block diagram of the model predictive control method proposed in Ref. [67] is shown in Fig. 10. Current research in this area primarily focuses on establishing the error estimation function, selecting the voltage vector, and calculating the duty cycle.

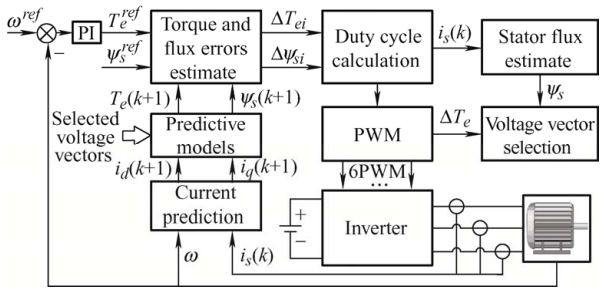

Fig. 10 Block diagram of model predictive control

4.2 Optimization of current harmonic

Another important component of torque ripple minimization based on the harmonic injection method is the calculation of current harmonics, which is generally solved based on the torque analytical model. In the actual solution process, according to the analytical model, countless combinations of current harmonics can suppress the torque ripple. Therefore, simplifications are generally made in the solution process, constraints are imposed, or the optimization objective is set to assist the solution progress.

In Ref. [23], for a surface-mounted PMSM without considering the inductance harmonics, only the flux harmonics were considered. If i_d=0, i_q can be obtained using the following equation

$$i_q = \frac{2\omega_e \overline{T_e}}{3pe_q} \tag{11}$$

where $\overline{T_e}$ is the average value of the torque after eliminating the ripples, e_q is the q-axis back electromotive force, and ω_e is the electric angular

velocity.

This method is only applicable to surface-mounted PMSMs and does not adequately suppress the torque ripple because the inductance harmonics and cogging torque are not considered.

In Ref. [24], only the 6th harmonics in the *d*-axis inductance L_d, *q*-axis inductance L_q, *d*-axis PM flux linkage ψ_{fd}, and *q*-axis PM flux linkage ψ_{fq} were considered. Subsequently, the resulting 6th and 12th harmonics of the torque ripple were eliminated. According to the calculations in this study, the current harmonics can be solved by solving nonlinear equations. However, the number of unknown variables to be solved is greater than the number of equations. Therefore, additional constraints were imposed, which are expressed as follows

$$\bar{i}_q = \frac{2\bar{T}_e}{3p\overline{\psi_{fd}}} \tag{12}$$

where $\bar{i}_q$ is the average value of the current i_q, and $\overline{\psi_{fd}}$ is the average value of ψ_{fd}.

The effect of Eq. (12) is to limit the solution range of i_q to $\bar{i}_q$, making the number of unknown variables equal to the number of nonlinear equations. This method requires an iterative approach to solve a set of nonlinear equations that are very complex to compute and can easily result in false solutions by entering a local minimum.

In Ref. [31], the cogging torque was considered. The reluctance torque ripple was ignored when solving the current harmonic, and the current ripple was assumed to exists only in i_q. The ripple-component i_q^r in i_q can be solved using the following equation

$$i_q^r = -\frac{p\overline{\boldsymbol{i}_{dq}^{\mathrm{T}}}\dfrac{\mathrm{d}\boldsymbol{\psi}_{fdq}}{\mathrm{d}\theta_e} + T_{cog}}{p\psi_d} \tag{13}$$

where the average *dq*-axis current vector is $\overline{\boldsymbol{i}_{dq}} = \left[\bar{i}_d \quad \bar{i}_q\right]^{\mathrm{T}}$ and the *dq*-axis PM flux vector is $\boldsymbol{\psi}_{fdq} = \left[\psi_{fd} \quad \psi_{fq}\right]^{\mathrm{T}}$.

This method inevitably results in a solution current that cannot completely eliminate the torque ripple because the reluctance torque is ignored. The results of this method cannot be applied under magnetic saturation because the analytical model does not consider magnetic saturation.

In Refs. [25, 28, 30, 55, 70], the concept of minimum current harmonics was proposed, all of which attempted to determine algorithms that can minimize the amplitude of the current harmonics. In Ref. [25], the minimum current harmonics were solved by setting the tangential direction of the torque contour line perpendicular to the current vector at different rotor positions, as shown in Fig. 11. The PMSM parameters differ at different rotor positions, resulting in different contour lines. For example, the torque contour lines are under θ_1 and θ_2 are $T_{\theta 1}$ and $T_{\theta 2}$. Subsequently, the current components i_d and i_q at different rotor positions are formed into a curve. The mathematical expression for the calculation is as follows

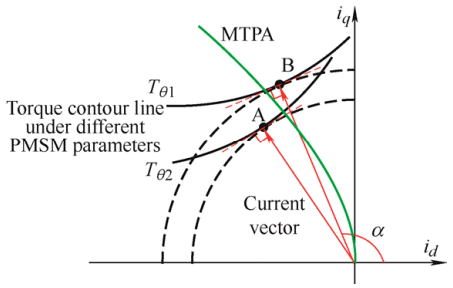

Fig. 11 Schematic of the minimum current harmonics method

$$\begin{bmatrix} -\dfrac{\partial T_e(\theta_e)}{\partial i_q} & \dfrac{\partial T_e(\theta_e)}{\partial i_d} \end{bmatrix} \begin{bmatrix} i_d \\ i_q \end{bmatrix} = 0 \tag{14}$$

Refs. [28, 30, 55] proposed that the minimum current harmonics can be obtained when the partial derivative of the torque to the angle α is zero at a certain electrical angle θ_e, as shown in the following equation

$$\frac{\partial T_e(\theta_e)}{\partial \alpha} = 0 \tag{15}$$

where α is the angle between the current vector and the *d*-axis in Fig. 11.

In Ref. [58], the coupling relationship between the f^{th} torque ripple harmonic component and $(f \pm 1)^{\mathrm{th}}$ current harmonic was derived in the harmonic category, as shown in the following equations

$$T_{ef}^c = \frac{3n_p}{4}\begin{bmatrix} \boldsymbol{i}_{dq1} \\ \boldsymbol{i}_{dqf-1} \\ \boldsymbol{i}_{dqf+1} \end{bmatrix}^{\mathrm{T}} \boldsymbol{L}_D^C \begin{bmatrix} \boldsymbol{i}_{dq1} \\ \boldsymbol{i}_{dqf-1} \\ \boldsymbol{i}_{dqf+1} \end{bmatrix} + \frac{3n_p}{2}\begin{bmatrix} \boldsymbol{i}_{dq1} \\ \boldsymbol{i}_{dqf-1} \\ \boldsymbol{i}_{dqf+1} \end{bmatrix}^{\mathrm{T}} \boldsymbol{\psi}_D^C + T_{cog}^c \tag{16}$$

$$T_{ef}^s = \frac{3n_p}{4}\begin{bmatrix} \boldsymbol{i}_{dq1} \\ \boldsymbol{i}_{dqf-1} \\ \boldsymbol{i}_{dqf+1} \end{bmatrix}^{\mathrm{T}} \boldsymbol{L}_D^S \begin{bmatrix} \boldsymbol{i}_{dq1} \\ \boldsymbol{i}_{dqf-1} \\ \boldsymbol{i}_{dqf+1} \end{bmatrix} + \frac{3n_p}{2}\begin{bmatrix} \boldsymbol{i}_{dq1} \\ \boldsymbol{i}_{dqf-1} \\ \boldsymbol{i}_{dqf+1} \end{bmatrix}^{\mathrm{T}} \boldsymbol{\psi}_D^S + T_{cog}^s \tag{17}$$

In the above two formulas, T_{ef}^{c}, T_{ef}^{s}, T_{cogf}^{c}, and T_{cogf}^{s} represent the sine and cosine components of the f^{th} torque and f^{th} cogging torque, respectively; $\boldsymbol{L}_{D}^{C}$, $\boldsymbol{\psi}_{D}^{C}$, $\boldsymbol{L}_{D}^{S}$, and $\boldsymbol{\psi}_{D}^{S}$ are the defined parameter matrices, which are calculated using the flux and inductance, respectively [58].

In Ref. [71], with the minimum amplitude of the injected $(f\pm1)^{\text{th}}$ current harmonics as the optimization objective, the minimum current harmonics analytical expression that can suppress the torque ripple was further derived according to the coupled torque-current harmonic equation given above. This method significantly reduces the computational difficulty and effectively avoids the problems of iterative operations and local minima. In Ref. [39], a genetic algorithm was proposed to solve for the minimum current harmonics, which also achieved good results.

The methods introduced above for calculating current harmonics depend on the premise of the given PMSM parameters. These parameters can be obtained using the FE method or experimental measurements. Regardless of which method is used, the current harmonic calculation is an open-loop feedforward calculation. Changing the temperature, degree of magnetic saturation, or PM aging results in a change in the PMSM parameters. The current harmonics will have a certain deviation. Refs. [57, 72-73] proposed the optimization of the current harmonics online using closed-loop control, in which the torque ripple is estimated by detecting the specific-order speed ripple. The minimum current harmonics that can suppress torque ripple can be obtained by continuous adjustment through online iterations. On one hand, the hardware cost of this method is relatively high; on the other hand, the adjustment process for torque ripple minimization is relatively long.

In current research, the current harmonic optimization direction for torque ripple minimization becomes more complicated. This is based on the principle of minimizing the current harmonic amplitude. For example, in Ref. [74], voltage fluctuation was considered during the optimization of the current harmonics to minimize the voltage fluctuation or the required DC voltage after harmonic injection as much as possible.

5 Conclusions

In this paper, the research status and latest progress in methods to minimize PMSM torque ripple based on harmonic injection are introduced. First, the causes of the PMSM torque ripple are analyzed. Subsequently, the research status of the PMSM torque analytical model is introduced. Finally, the research status of the harmonic control and current harmonic optimization methods in minimizing PMSM torque ripple based on harmonic injection is discussed in detail. This paper aims to provide guidance for PMSM torque ripple minimization. Although torque ripple minimization based on harmonic injection can overcome many problems that cannot be solved using methods based on improving the electromagnetic structure, it has some inherent limitations. For example, it has higher requirements for current control, high requirements for the motor model and parameter accuracy to achieve a good torque ripple minimization effect, and higher requirements for voltage modulation and DC voltage amplitude. In response to the above challenges, the limitations and possible improvements of the current research are summarized as follows.

(1) Decomposition of current harmonics. To perform closed-loop control on the current harmonics, we must accurately obtain the amplitude and phase information of the current harmonic. Currently, harmonic decomposition methods are primarily implemented using low-pass filters. However, this method produces delays in the dynamic process. As the harmonic orders increase, the delay characteristics significantly affect the stability of the controller. Therefore, rapid and accurate decomposition of current harmonics is an important research topic.

(2) Optimization of current harmonics. Current harmonic injection has many unwanted effects, such as increasing the PMSM loss and decreasing the voltage utilization ratio. Therefore, in the current harmonic optimization process, more factors should be considered to seek a multi-objective linkage to achieve better optimization.

(3) Acquisition of accurate PMSM parameters. Motor parameters have a significant influence on the calculation of current harmonics and the dynamic process of harmonic control. PMSM parameters are

affected by temperature, aging, and other factors. However, obtaining the harmonic parameters is difficult. Therefore, obtaining accurate motor parameters is an important part of this research.

(4) Problems with high-speed harmonic injection. Currently, high-speed PMSMs represent one of the most important developmental trends. This introduces several control problems. For example, the delay characteristics in the control (PWM delay, current sampling delay, and delay produced by harmonic decomposition) significantly affect the harmonic injection effect at high speeds. Moreover, when the fundamental frequency of the current is high, harmonic injection becomes more difficult because of the limitation of the PWM switching frequency. Therefore, the realization of harmonic injection at high speeds is an important research topic.

References

[1] D Wang, C Peng, X Wang. Research on different design approaches to mitigate torque ripple and electromagnetic vibration for high-performance electric vehicle traction machine. *Journal of Electrical Engineering*, 2021, 16(4): 42-49.

[2] W Chu, Z Zhu. Investigation of torque ripples in permanent magnet synchronous machines with skewing. *IEEE Transactions on Magnetics*, 2013, 49(3): 1211-1220.

[3] M Zhou, X Zhang, W Zhao, et al. Influence of magnet shape on the cogging torque of a surface-mounted permanent magnet motor. *Chinese Journal of Electrical Engineering*, 2019, 5(4): 40-50.

[4] C M Spargo, B C Mecrow, J D Widmer. A seminumerical finite-element postprocessing torque ripple analysis technique for synchronous electric machines utilizing the air-gap Maxwell stress tensor. *IEEE Transactions on Magnetics*, 2014, 50(5): 1-9.

[5] K Wang, Z Zhu, G Ombach, et al. Average torque improvement of interior permanent-magnet machine using third harmonic in rotor shape. *IEEE Transactions on Industrial Electronics*, 2014, 61(9): 5047-5057.

[6] J Liang, A Parsapour, Z Yang, et al. Optimization of air-gap profile in interior permanent-magnet synchronous motors for torque ripple mitigation. *IEEE Transactions on Transportation Electrification*, 2019, 5(1): 118-125.

[7] L Alberti, M Barcaro, N Bianchi. Design of a low torque ripple fractional-slot interior permanent magnet motor. *IEEE Transactions on Industry Applications*, 2014, 50(3): 1801-1808.

[8] G Wang, Y Yu, R Yang, et al. Dead-time compensation of space vector PWM inverter for induction motor. *Proceedings of the CSEE*, 2008, 28(15): 79-83.

[9] S H Hwang, J M Kim. Dead time compensation method for voltage-fed PWM inverter. *IEEE Transactions on Energy Conversion*, 2010, 25(1): 1-10.

[10] J Yu, P Zhu, Y Xu. Dead zone compensation strategy for inverter of PMSM based on direct axis voltage analysis. *Journal of Electrical Engineering*, 2021, 16(4): 51-58.

[11] N Bedetti, S Calligaro, R Petrella. Self-commissioning of inverter dead-time compensation by multiple linear regression based on a physical model. *IEEE Transactions on Industry Applications*, 2015, 51(5): 3954-3964.

[12] G Liu, D Wang, Y Jin, et al. Current detection independent dead-time compensation method based on terminal voltage A/D conversion for PWM VSI. *IEEE Transactions on Industrial Electronics*, 2017, 64(10): 7689-7699.

[13] D H Lee, J W Ahn. A simple and direct dead-time effect compensation scheme in PWM-VSI. *IEEE Transactions on Industry Applications*, 2014, 50(5): 3017-3025.

[14] Y Liao, J Yao, S Yang. Analysis and elimination method of harmonics produced by forward voltage drop of ACEG excitation power source. *Proceedings of the CSEE*, 2004, 24(4): 151-156.

[15] J T Boys, P G Handley. Harmonic analysis of space vector modulated PWM waveforms. *IEE Proceedings*, 1990, 137(4): 197-204.

[16] Y Huang, Y Xu, W Zhang, et al. Hybrid RPWM technique based on modified SVPWM to reduce the PWM acoustic noise. *IEEE Transactions on Power Electronics*, 2019, 34(6): 5667-5674.

[17] P Yi, Y Yin, X Wang, et al. PMSM torque ripple minimization based on novel low carrier ratio PWM technique. *IEEE Transactions on Power Electronics*, 2022, 37(9): 11071-11084.

[18] Y Huang, Y Xu, W Zhang, et al. Modified single-edge SVPWM technique to reduce the switching losses and increase PWM harmonics frequency for three-phase VSIs. *IEEE Transactions on Power Electronics*, 2020, 35(10): 10643-10653.

[19] V S S P K Hari, G Narayanan. Space-vector-based hybrid PWM technique to reduce peak-to-peak torque ripple in induction motor drives. *IEEE Transactions on Industry*

Applications, 2015, 52(2): 1489-1499.

[20] W Liang, J Wang, P C K Luk, et al. Analytical modeling of current harmonic components in PMSM drive with voltage-source inverter by SVPWM technique. *IEEE Transactions on Energy Conversion*, 2014, 29(3): 673-680.

[21] I Jeong, K Nam. Analytic expressions of torque and inductances via polynomial approximations of flux linkages. *IEEE Transactions on Magnetics*, 2015, 51(7): 1-9.

[22] A Piippo, J Luomi. Torque ripple reduction in sensorless PMSM drives. *32nd Annual Conference on IEEE Industrial Electronics (IECON 2006)*, November 6-10, 2006, Paris, France. Piscataway: IEEE, 2006: 920-925.

[23] P Mattavelli, L Tubiana, M Zigliotto. Torque-ripple reduction in PM synchronous motor drives using repetitive current control. *IEEE Transactions on Power Electronics*, 2005, 20(6): 1423-1431.

[24] A Madani, J P Barbot, F Colamartino, et al. Reduction of torque pulsations by inductance harmonics identification of a permanent-magnet synchronous machine. *Proceedings of the 1995 IEEE Conference on Control Applications*, September 28-29, 1995, Albany, NY, USA. Piscataway: IEEE, 1995: 787-792.

[25] C Marchand, A Razek. Optimal torque operation of digitally controlled permanent magnet synchronous motor drives. *IEE Proceedings-B Electric Power Applications*, 1993, 140(3): 232-240.

[26] G H Lee, S I Kim, J P Hong, et al. Torque ripple reduction of interior permanent magnet synchronous motor using harmonic injected current. *IEEE Transactions on Magnetics*, 2008, 44(6): 1582-1585.

[27] L Springob, J Holtz. High-bandwidth current control for torque-ripple compensation in PM synchronous machines. *IEEE Transactions on Industrial Electronics*, 1998, 45(5): 713-721.

[28] F Colamartino, C Marchand, A Razek. Torque ripple minimization in permanent magnet synchronous servodrive. *IEEE Transactions on Energy Conversion*, 1999, 14(3): 616-621.

[29] H Jia, M Cheng, W Hua, et al. Cogging torque compensation for flux-switching permanent magnet motor based on current harmonics injection. *Proceedings of the CSEE*, 2009, 29(27): 83-89.

[30] N Nakao, K Akatsu. Torque ripple suppression of permanent magnet synchronous motors considering total loss reduction. *5th Annual IEEE Energy Conversion Congress and Exhibition (ECCE 2013)*, September 15-19, 2013, Denver, CO, USA. Washington: IEEE, 2013: 3880-3887.

[31] N Nakao, K Akatsu. Suppressing pulsating torques: Torque ripple control for synchronous motors. *IEEE Industry Applications Magazine*, 2014, 20(6): 33-44.

[32] J Holtz, L Springob. Identification and compensation of torque ripple in high-precision permanent magnet motor drives. *IEEE Transactions on Industrial Electronics*, 1996, 43(2): 309-320.

[33] J Tan. Selection of slot/pole number combinations for BLDCM with concentrated windings. *Micromotors*, 2008, 2008(2): 74-79.

[34] S Wang, J Kang, M Zhong, et al. Overviews of torque ripple suppression method with permanent magnet synchronous motor used in electric vehicles. *Journal of Power Supply*, 2016, 14(5): 24-32.

[35] H Che, E Levi, M Jones, et al. Current control methods for an asymmetrical six-phase induction motor drive. *IEEE Transactions on Power Electronics*, 2014, 29(1): 407-417.

[36] R Bojoi, F Farina, M Lazzari, et al. Analysis of the asymmetrical operation of dual three-phase induction machines. *IEEE International Electric Machines and Drives Conference (IEMDC 2003)*, June 1-4, 2003, Madison, WI, USA. Piscataway: IEEE, 2003: 429-435.

[37] R J Strahan. Energy conversion by nonlinear permanent magnet machines. *IEE Proceedings-Electric Power Applications*, 1998, 145(3): 193-198.

[38] J Li, Y Yong. Model of permanent magnet synchronous motor considering saturation and rotor flux harmonics. *Proceedings of the CSEE*, 2011, 31(3): 60-66.

[39] C Lai, G Feng, K Mukherjee, et al. Torque ripple modeling and minimization for interior PMSM considering magnetic saturation. *IEEE Transactions on Power Electronics*, 2017, 33(3): 2417-2429.

[40] I Boldea, S A Nasar. A general equivalent circuit (GEC) of electric machines including cross-coupling saturation and frequency effects. *IEEE Transactions on Energy Conversion*, 1988, 3(3): 689-695.

[41] B Stumberger, G Stumberger, D Dolinar, et al. Evaluation of saturation and cross-magnetization effects in interior permanent-magnet synchronous motor. *IEEE Transactions on Industry Applications*, 2003, 39(5): 1264-1271.

[42] H Li, J Zhang, Y Luo. Finite element analysis of PMSM steady state parameters considering cross-saturation effect. *Proceedings of the CSEE*, 2012, 32(12): 104-110.

[43] J F Gieras, E Santini, M Wing. Calculation of synchronous reactances of small permanent-magnet alternating-current motors: Comparison of analytical approach and finite element method with measurements. *IEEE Transactions on Magnetics*, 1998, 34(5): 3712-3720.

[44] H Li, J Zhang, M Liu. An improved calculation method for steady-state parameters of PMSM with T-S FEM. *Transactions of China Electrotechnical Society*, 2012, 27(4): 35-41.

[45] X Wang, P Yi, Z Zhou, et al. Improvements in the permanent magnet synchronous motor torque model using incremental inductance. *IET Electric Power Applications*, 2020, 14(1): 109-118.

[46] Z Zhong, S Jiang, Y Zhou, et al. Active torque ripple reduction based on an analytical model of torque. *IET Electric Power Applications*, 2017, 11(3): 331-341.

[47] W Tong, S Li, X Pan, et al. Analytical model for cogging torque calculation in surface-mounted permanent magnet motors with rotor eccentricity and magnet defects. *IEEE Transactions on Energy Conversion*, 2020, 35(4): 2191-2200.

[48] L Wu, Z Zhu, D A Staton, et al. Comparison of analytical models of cogging torque in surface-mounted PM machines. *IEEE Transactions on Industrial Electronics*, 2012, 59(6): 2414-2425.

[49] K Zhang, Y Kang, J Xiong, et al. Direct repetitive control of SPWM inverters for UPS purpose. *IEEE Transactions on Power Electronics*, 2003, 18(3): 784-792.

[50] T Jahns, W Soong. Pulsating torque minimization techniques for permanent magnet AC motor drives: A review. *IEEE Transactions on Industrial Electronics*, 1996, 43(2): 321-330.

[51] A G Yepes, F D Freijedo, Ó Lopez , et al. Analysis and design of resonant current controllers for voltage-source converters by means of nyquist diagrams and sensitivity function. *IEEE Transactions on Industrial Electronics*, 2011, 58(11): 5231-5250.

[52] J Gao, X Wu, S Huang, et al. Torque ripple minimisation of permanent magnet synchronous motor using a new proportional resonant controller. *IET Power Electronics*, 2017, 10(2): 208-214.

[53] C Xia, B Ji, Y Yan. Smooth speed control for low-speed high-torque permanent-magnet synchronous motor using proportional-integral-resonant controller. *IEEE Transactions on Industrial Electronics*, 2015, 62(4): 2123-2134.

[54] H Chuan, S M Fazeli, Z Wu, et al. Mitigating the torque ripple in electric traction using proportional integral resonant controller. *IEEE Transactions on Vehicular Technology*, 2020, 69(10): 10820-10831.

[55] B Guan, Y Zhao, Y Ruan. Torque ripple minimization in interior PM machines using FEM and multiple reference frames. *2006 1st IEEE Conference on Industrial Electronics and Applications (ICIEA 2006)*, May 24-26, 2006, Singapore, Singapore. Piscataway: IEEE, 2006: 1-6.

[56] Y Liao, S Zhen, R Liu. Torque ripple suppression of permanent magnet synchronous motor by the harmonic injection. *Proceedings of the CSEE*, 2011, 31(21): 119-127.

[57] G Feng, C Lai, N C Kar. Speed harmonic based decoupled torque ripple minimization control for permanent magnet synchronous machine with minimized loss. *IEEE Transactions on Energy Conversion*, 2020, 35(4): 1796-1805.

[58] P Yi, X Wang, Z Sun. Research on PMSM harmonic coupling models based on magnetic co-energy. *IET Electric Power Applications*, 2019, 13(4): 571-579.

[59] P Yi, X Wang, D Chen, et al. PMSM current harmonics control technique based on speed adaptive robust control. *IEEE Transactions on Transportation Electrification*, 2022, 8(2): 1794-1806.

[60] S Jiang, Y Wang. Internal mode decoupled harmonic current tracking for vehicular PMSMs noise reduction. *IEEE Transactions on Vehicular Technology*, 2022, 71(12): 12711-12721.

[61] F Morel, X Linshi, J Retif, et al. A comparative study of predictive current control schemes for a permanent-magnet synchronous machine drive. *IEEE Transactions on Industrial Electronics*, 2009, 56(7): 2715-2728.

[62] Y Zhang, H Yang. Two-vector-based model predictive torque control without weighting factors for induction motor drives. *IEEE Transactions on Power Electronics*, 2016, 31(2): 1381-1390.

[63] X Wang, D Sun. Three-vector-based low-complexity model predictive direct power control strategy for doubly fed induction generators. *IEEE Transactions on Power Electronics*, 2017, 32(1): 773-782.

[64] Z Zhou, C Xia, Y Yan, et al. Torque ripple minimization of predictive torque control for PMSM with extended control set. *IEEE Transactions on Industrial Electronics*, 2017, 64(9): 6930-6939.

[65] X Yuan, C Zhang, S Zhang. Torque ripple suppression for open-end winding permanent-magnet synchronous machine drives with predictive current control. *IEEE Transactions on Industrial Electronics*, 2019, 67(3): 1771-1781.

[66] M N Uddin, M M Rahman. Online torque-flux estimation-based nonlinear torque and flux control scheme of IPMSM drive for reduced torque ripples. *IEEE Transactions on Power Electronics*, 2019, 34(1): 636-645.

[67] X Li, Z Xue, L Zhang, et al. A low-complexity three-vector-based model predictive torque control for SPMSM. *IEEE Transactions on Power Electronics*, 2021, 36(11): 13002-13012.

[68] X Li, Z Xue, X Yan, et al. Low-complexity multivector-based model predictive torque control for PMSM with voltage preselection. *IEEE Transactions on Power Electronics*, 2021, 36(10): 11726-11738.

[69] L Chen, H Xu, X Sun, et al. Three-vector-based model predictive torque control for a permanent magnet synchronous motor of EVs. *IEEE Transactions on Transportation Electrification*, 2021, 7(3): 1454-1465.

[70] G Feng, C Lai, N C Kar. An analytical solution to optimal stator current design for PMSM torque ripple minimization with minimal machine losses. *IEEE Transactions on Industrial Electronics*, 2017, 64(10): 7655-7665.

[71] P Yi, X Wang, Z Sun. Interior permanent magnet synchronous motor minimum current harmonics torque ripple suppression strategy based on magnetic co-energy model. *IET Electric Power Applications*, 2020, 14(2): 234-244.

[72] G Feng, C Lai, N C Kar. Practical testing solutions to optimal stator harmonic current design for PMSM torque ripple minimization using speed harmonics. *IEEE Transactions on Power Electronics*, 2018, 33(6): 5181-5191.

[73] L Yan, Y Liao, H Lin, et al. Torque ripple suppression of permanent magnet synchronous machines by minimal harmonic current injection. *IET Power Electronics*, 2019, 12(6): 1368-1375.

[74] X Wang, H Wang, Y Liu, et al. Multi-objective control harmonic current solution for permanent magnet synchronous motor. *2022 IEEE Transportation Electrification Conference and Expo*, *Asia-Pacific (ITEC Asia-Pacific 2022)*, October 28-31, 2022, Haining, China. Piscataway: IEEE, 2022: 1-6.

Peng Yi received the B.S. degree in Automotive Engineering from Jilin University, Changchun, China in 2011, M.S. and Ph.D. degrees in Automotive Engineering from Tongji University, Shanghai, China in 2014 and 2020, respectively. He has been with the College of Electrical Engineering of Qingdao University since 2020. His current research interests include torque ripple minimization, loss characteristics and electromagnetic vibration of PMSM.

Wenzhi Zheng received the B.S. degree in Electrical Engineering from Qingdao University, Shandong Province, China in 2021 and is currently pursuing the M.S. degree in Electrical Engineering from Qingdao University. His current research direction is electromagnetic vibration of PMSM used in electrical vehicle.

Xianglin Li (M'15) received the B.S. and M.S. degrees from China University of Petroleum (East China), Qingdao, China, in 2007 and 2010, respectively, and the Ph.D. degree from Southeast University, Nanjing, China, in 2015, all in Electrical Engineering. He was a joint-supervised Ph.D. student with the Wisconsin Electric Machine and Power Electronics Consortium (WEMPEC), University of Wisconsin-Madison, Madison, WI, USA, from Sept. 2012 to Sept. 2013, and a Research Assistant with the Department of Electrical and Electronic Engineering, University of Hong Kong, Hong Kong, China, from Jul. 2014 to Jan. 2015.

From 2015 to 2019, he was an Associate Professor with China University of Petroleum (East China). Since 2020, he has been a Professor in the College of Electrical Engineering, Qingdao University. His research interests mainly include design, analysis, and control of electrical machines, especially for PM brushless machines and high temperature superconducting machines, etc.